X-ray CT-derived soil characteristics explain varying air, water and solute transport properties across a loamy field

Marcos Paradelo*[1,2], Sheela Katuwal[1], Per Moldrup[3], Trine Norgaard[1], Lasantha Herath[1], and Lis W. de Jonge[1]

[1]Dept. of Agroecology, Faculty of Sciences and Technology, Aarhus University, Blichers Allé 20, P.O. Box 50, DK-8830 Tjele, Denmark

[2]Dept. of Plant Biology and Soil Science, Faculty of Sciences, University of Vigo, E-32004 Ourense, Spain

[3]Dept. of Civil Engineering, Aalborg University, Sofiendalsvej 11, DK-9200 Aalborg SV, Denmark

* corresponding author e-mail address: marcos.paradelo@agro.au.dk

ABSTRACT

The characterisation of soil pore space geometry is important for explaining fluxes of air, water and solutes through soil and understanding soil hydrogeochemical functions. X-ray computed tomography (CT) can be applied for this characterization, and in this study CT-derived parameters were used to explain water, air and solute transport through soil.

Forty-five soil columns (20-cm × 20-cm) were collected from an agricultural field in Estrup, Denmark, and subsequently scanned using a medical CT scanner. Non-reactive tracer leaching experiments were performed in the laboratory along with measurements of air permeability (K_a), and saturated hydraulic conductivity (K_{sat}). The CT number of the matrix (CT_{matrix}), which represents the moist bulk density of the soil matrix, was obtained from the CT scans as the average CT number of the voxels in the greyscale image excluding macropores and stones. The CT_{matrix} showed the best relationships with the solute transport characteristics, especially the time by which 5 % of the applied mass of tritium was leached, known as 5% arrival time ($t_{0.05}$). CT-derived macroporosity (pores larger than 1.2 mm) was correlated with K_a and $\log_{10}(K_{sat})$. The correlation improved when limiting macroporosity (the minimum macroporosity for every 0.6 mm layer along the soil column) was used, suggesting that soil layers with the narrowest macropore section restricted the flow through the whole soil column. Water, air and solute transport were related with the CT-derived parameters by using a best subsets regression analysis. The regression coefficients improved using CT_{matrix}, limiting macroporosity and genus density while the best model for $t_{0.05}$ used CT_{matrix} only. The scanning resolution and the time for soil structure development after mechanical activities could be factors that increased the uncertainty of the relationships. Nevertheless, the results confirmed the potential of X-ray CT visualisation techniques for estimating fluxes through soil at field-scale.

INTRODUCTION

Linking pore space geometry with the fluxes of air, water and solutes through soil is fundamental for understanding the processes that control soil functions such as water storage, gas exchange and contaminant filter potential. Macropores in soils are often associated with high variabilities in the transmission of air, water and solutes through soils. Macropores are pores with diameters larger than 0.3-0.5 mm and formed from earthworm burrows, decaying plant roots, swelling/shrinkage cracks or inter-aggregate voids (Jarvis, 2007). Even though they only constitute a small fraction of the soil (Jarvis, 2007), air and water can move preferentially within the soil's macropores. Iversen et al. (2001a) found higher variability of air and water flow in structured loamy soils than in sandy soils, where macropores are not present. The size and connectivity of the pores affect advective air transport through soil (Ball, 1981), and therefore air permeability measurements were used to investigate macropore geometry (Roseberg and Mccoy, 1990). It is well known that macropore flow together with the movement of colloids (as carriers) can facilitate the rapid transport of strongly sorbed contaminants (de Jonge et al., 2004a, McCarthy and Zachara, 1989, Schelde et al., 2006). Thus agrochemicals and e.g. particulate phosphorus, that are believed to have low mobility in soil, have been detected in tile drains (de Jonge et al., 2004b, Norgaard et al., 2014, Traub-Eberhard et al., 1995). Many studies have tried to assess the importance of macropore flow using pore size distribution or macropore shape, and developed pedotransfer functions to estimate the occurrence of preferential flow from measured soil properties. Iversen et al. (2012) found that macropore flow at saturated conditions was strongly correlated with macropore density in soils covering the different geological regions of Denmark. Soil texture and organic carbon content are considered to be important factors governing air and water flow, but other parameters such as bulk density, water saturation state, lateral scale or soil management should also be considered (Jarvis et al., 2009, Koestel and Jorda, 2014, Koestel et al., 2013).

Since the 1980s, and much more in the past decade, non-invasive techniques have been developed to be used in soil hydrology and other geophysical sciences. Imaging techniques such as nuclear magnetic resonance imaging (MRI), dual-energy gamma radiation or X-ray computed tomography (CT) are used to characterize pore network, colloid dynamics and solute transport through porous media (Werth et al., 2010). X-ray CT is becoming increasingly attractive due to improvements in resolution and access to industrial, medical and benchtop scanners (Vaz et al., 2011), providing tools for visualising and quantifying the 3D inner structure of the soil. Among other applications, X-ray CT has been used to characterise pore space geometry and estimate bulk density, pore tortuosity, water content, root-soil interactions, biomass distribution, soil mechanical properties and solute transport. Review of X-ray CT applications in soil science and geoscience can be found in numerous papers (Helliwell et al., 2013, Ketcham and Carlson, 2001, Taina et al., 2008, Wildenschild et al., 2002).

It is clear that X-ray CT can be useful for quantifying macropore characteristics and soil structure and linking them with soil fluxes. In the last few years, researchers have tried to establish links between X-ray CT-derived measurements and transport properties such as air permeability, hydraulic conductivity and solute dispersivity. In soils with two different land uses, Luo et al. (2010b) have found that saturated hydraulic conductivity (K_{sat}) is correlated with macroporosity and path number (number of independent and continuous macropore paths between two boundaries). They also found that dispersivity is correlated with the path number, hydraulic radius and macropore angle (angle away from vertical to characterize the inclination of a macropore). Macroporosity and limiting macroporosity (minimum macroporosity along the soil column) were found to be good predictors of air permeability at -3 kPa matric potential in undisturbed soils from a clay gradient field (Naveed et al., 2013). The degree of preferential flow and the release of copper in a polluted soil have been estimated from the macroporosity derived from X-ray CT images (Paradelo et al., 2013). Larsbo et al. (2014) have also found significant relationships between the degree of preferential flow and the CT derived macropore characteristics like macroporosity, macropore surface area, aggregate thickness and connectivity. Most recently, two studies reported a relationship between coarse-resolution CT scans and solute transport experiments on 20 cm × 20 cm undisturbed soil columns collected in two loamy fields in Denmark. In the first study, the air permeability at -2 kPa matric potential and 5% arrival time, the time by which the 5% of the applied mass of a tracer is leached, were estimated from coarse-resolution CT images by identifying macropores between 5 and 25 % of the air-filled porosity at -2 kPa matric potential (Katuwal et al., 2015b). Here, the best parameters were macroporosity and limiting macroporosity. In the second study, the CT number-derived matrix density is introduced as a new parameter for determining the degree of preferential flow (Katuwal et al., 2015a) and defined as the average CT number of the voxels in the greyscale image excluding macropores and stones.

Current literature proves the suitability of X-ray CT visualisation and image characterization for explaining air and water fluxes through the soil, but more work needs to be done to produce universal models. The strong correlation between most X-ray CT-derived characteristics can limit the amount of useful information required for modelling purposes (Larsbo, et al., 2014, Luo, et al., 2010b). The present study aims to explain the variations in water, air and solute transport in an agricultural loamy field in Denmark using CT-derived characteristics. The findings will help to evaluate the potential of X-ray CT technics to explain the field-scale variability of flow and transport processes. Forty-five intact soil samples were taken in a regular grid from the field and scanned using a medical scanner with a coarse resolution (1.2 mm). The relationships between transport characteristics and CT-derived parameters were developed using simple and multiple linear regressions.

MATERIAL AND METHODS

Field site and sampling

Soil sampling was carried out at a 1.26 ha agricultural field in Estrup (55°29´09.96´´N, 9°04´09.37´´E), Denmark (Fig. 1A). The field is a part of the Danish Pesticide Leaching Assessment Programme (Lindhardt et al., 2001). Three pedological profiles within the Estrup field were classified as Aquic Argiudoll, Abruptic Argiudoll and Fragiaquic Glossudalf (Lindhardt, et al., 2001, Soil Survey Staff, 1999). The management of the field prior to sampling comprised of ploughing to a 20-cm depth plus ring roller packing (November 2011), rotor harrowing at a 4 cm depth and spring barley seeding with a row distance of 12 cm (March 2012), followed by harvesting (August 2012).

In September 2012, forty-five undisturbed soil columns were sampled from a 15 m × 15 m grid (Fig. 1B). Cylindrical aluminium rings (20-cm × 20-cm) were carefully pushed into the soil by a hydraulic press mounted on a tractor. The soil surrounding the ring was manually excavated, the core extracted and the bottom carefully cut. Plastic lids covered the top and bottom ends. The samples were transported to the laboratory and stored at 2 °C until further analyses (X-ray CT scanning, air permeability, solute transport and hydraulic conductivity). In addition, bulk soil was collected at each sample point, air dried and sieved through 2 mm in the laboratory for the measurement of texture and organic carbon (OC).

Basic soil properties

The texture was determined by a combined sieve/hydrometer method (Gee and Or, 2002). Organic carbon was determined by a LECO analyser coupled with an infrared CO_2 detector (Thermo Fisher Scientific Inc., MA, USA).

Image acquisition, processing and segmentation

A medical scanner (Siemens Biograph™ TruePoint™ 64) was used to scan the soil columns at *in situ* soil moisture conditions. An energy level of 120 kV, exposure of 740 mAs and X-ray tube current of 333 mA were applied to acquire the images. 16-bit images with a pixel size of 0.4297 x 0.4297 mm and a slice thickness of 0.6 mm were obtained. The image greyscale was normalized to Hounsfield units (HU) and referred to as the CT number in the following. The CT number depends on the electron density which is very closely related to the bulk density for a given energy (Anderson et al., 1988).

The images were processed using the Avizo Fire 7® software package (FEI Visualization Sciences Group, Burlington, MA, USA) and ImageJ version 1.47h (Abramoff et al., 2004, Ferreira and Rasband, 2012). First the images were cropped to obtain a region of interest (ROI) of 18 cm in diameter and 17 cm high. The brightness and contrast of the images were then adjusted, and transformed to 8-bit grey scale to apply the locally adaptive segmentation method proposed by Sauvola and Pietikäinen (2000) in ImageJ. The segmentation method is based on the calculation of the threshold (*T*) for each pixel in the image using the information of the neighbouring pixels as:

$$T(x,y) = m(x,y) \cdot \left[1 + k\left(\frac{s(x,y)}{R} - 1\right)\right] \qquad [1]$$

where $m(x, y)$ and $s(x, y)$ are the local mean and standard deviation of the pixel intensities in the neighbourhood of the pixel whose threshold value is computed, R is the maximum standard deviation and k is a constant with a positive value. The default values of k=0.5 and R=128 and a neighbourhood with a radius of 15 pixels provided the best segmentation results which was assessed by visual inspection. The segmentation produced binary images where a set of connected voxels represented a pore feature. All features smaller than two voxels in width (minimum Feret diameter <1.2 mm) were removed from the segmented binary data to prevent the classification of noise as pores. Thus the pores detected and quantified using X-ray CT were ≥ 1.2 mm in width and are denoted as macropores in the following. Stones were segmented based on the global intensity histogram in which a second order polynomial was fitted between the peaks indicative of the soil matrix (about 1000 HU) and stones (about 2000 HU) adjusting the range. The minimum of the polynomial was taken as the threshold value for the stones.

CT-derived macroporosity, limiting macroporosity, macropore connectivity and CT_{matrix}

CT-derived macroporosity was calculated by dividing the total number of voxels classified as pores by the total number of voxels present within the ROI. The macroporosity distribution with depth was obtained by calculating the macroporosity for each 0.6 mm slice of the CT data along the soil depth. The minimum value of macroporosity along the soil depth, corresponding to the major flow direction was referred to as the limiting macroporosity. For quantifying the connectivity of the macropores, the density of loops or redundant connections, also known as genus density (Vogel et al., 2010), within the ROI was measured using the BoneJ Particle Analyzer plugin (version 1.3.11) in ImageJ (Doube et al., 2010). The average CT number of the matrix (CT_{matrix}), which is closely related to the wet density of the samples, was obtained as the average CT number of the voxels in the greyscale image within the ROI, excluding the voxels comprising the macropores and stones. Furthermore the average CT number of the matrix for each slice along the soil depth was also calculated.

Air, water and solute transport

The air permeability of the soil columns was measured at *in situ* soil moisture conditions ($K_{a\_(in\ situ)}$) using an air permeameter developed by Iversen et al. (2001b). Briefly, a constant pressure of 5 cm water column was applied to the top of the column, and the velocity at which the air passes through the soil was measured using a connected flow meter.

The soil columns were slowly saturated from the bottom for three days with artificial soil water (0.652 mM NaCl, 0.025 mM KCl, 1.842 mM $CaCl_2$ and 0.255 mM $MgCl_2$; pH = 6.38; EC = 0.6 mS cm^{-1}) and then drained for three days to -2 kPa matric potential at the centre of the column (-1 kPa at the bottom). Air permeability was again measured at this potential ($K_{a\ (-2kPa)}$).

The soil columns were then placed on a 1-mm stainless steel screen and irrigation was performed using a rotating head with 44 needles placed randomly to ensure a homogeneous distribution on the soil surface. Artificial rain water (0.012 mM $CaCl_2$, 0.015 mM $MgCl_2$ and 0.121 mM NaCl; pH = 6.5; EC = 0.025 mS cm^{-1}) was applied by a peristaltic pump with an intensity equal to 10 mm h^{-1}. Seepage face boundary condition was set at the bottom of the columns. After steady flow had been reached at the bottom of the columns (approximately 50 min after the start of the experiment), a 10-min pulse of tritium was applied at the same intensity (10 mm h^{-1}). The columns were irrigated for a total time of eight hours. The effluent was collected at different time intervals in plastic bottles by an automated fraction collector. To determine the tritium concentration in the effluent samples, 1 mL of each sample was mixed with 2 mL of water and 17 mL of scintillation cocktail (Packard Ultima Gold). Tritium was then quantified using a liquid scintillation analyser (Packard 2250 CA, Downers Grove, IL). The tritium breakthrough curves (BTC) were constructed for each soil column representing the relative concentration of tritium in the effluent *versus* time. The forty-five leaching experiments were performed between February and June 2013.

After the breakthrough experiments, the saturated hydraulic conductivity (K_{sat}) was measured using the constant head method (Klute and Dirksen, 1986). Finally the soil columns were oven-dried at 105 °C and weighed in order to obtain their bulk densities.

Breakthrough shape characteristics

The solute transport was described by two measures of the solute breakthrough shape, 5% arrival time and apparent dispersivity. The 5% arrival time ($t_{0.05}$) is the time when 5% of the tracer applied to the top of the column is collected in the effluent, and indicates a tendency for early arrival of the solutes. Knudby and Carrera (2005) and later Koestel et al. (2011) proposed the relative 5% arrival time as a robust measure of preferential transport; using relative times allows to compare BTCs from different sizes and experimental conditions. Since all the experiments where running with same soil sample size and flow rate absolute 5% arrival time will be used in this work. The apparent dispersivity is a measure for the variance of transport velocities in the soil (Koestel, et al., 2011).

Regarding that some experimental tritium BTCs can be bimodal, they were fitted to a mix of two lognormal probability density functions (PDF):

$$f(t) = w_1 g_1(t) + w_2 g_2(t) \quad [2]$$

where w_1 and w_2 are the weighing factors that add up to one, and g_1 and g_2 are the lognormal distribution functions of the form:

$$g(t) = \frac{1}{\sqrt{2\pi}\,\sigma t}\, exp\left[-\frac{(\ln t - \mu)^2}{2\sigma^2}\right] \quad [3]$$

where t is the time (h), μ is the mean of ln(t) (dimensionless) and σ (dimensionless) is the standard deviation (Jury and Roth, 1990). Temporal moments were calculated from the fitted PDF by:

$$m_j = \int_0^{\infty} t^j\, f\, \mathrm{d}t \quad [4]$$

where t is time (h), m_j is the jth temporal moment and f is the PDF. The normalised first temporal moment, μ_1' (h), is defined as m_1/m_0. From μ_1' the normalised temporal moments were calculated as:

$$m_j = \frac{1}{m_0 \mu_1'^{\,j}} \int_0^{\infty} (t - \mu_1')^j\, f\, \mathrm{d}t \quad [5]$$

Apparent dispersivity, λ_{app}, was defined by the travel distance, *L*, and the second central temporal moment, μ_2:

$$\lambda_{app} = \frac{\mu_2 L}{2} \quad [6]$$

The $t_{0.05}$ was calculated as:

$$t_{0.05} = p_{0.05}\mu_1' \quad [7]$$

where $p_{0.05}$ denotes the 5% quantile of the transfer function (Koestel, et al., 2011).

Statistics

Spearman rank coefficients (r) were calculated to assess the relationships between soil characteristics, CT-derived characteristics and air, water and solute transport parameters. Contour plot of OC content was constructed using empirical Bayesian kriging in ArcMap 10.1.

Best subsets regression procedure was performed to examine the relationship of CT-derived parameters with the air, water and solute transport characteristics. Best subset regression selects variables in a multiple linear regression by systematically searching through all different combinations of the independent variables and selecting the subsets of variables that best predict the dependent variable. The best subset was selected by comparing R^2, adjusted R^2 and Mallows's Cp; as criterion to prevent overfitting when additional variables are added (Hocking, 1976), using the statistical software Sigmaplot 11.0 (Systat Software, Inc., San Jose – CA, USA). When the best subset was selected, residuals of the model were tested for normality (Shapiro-Wilk test) and homoscedasticity.

RESULTS AND DISCUSSION

Soil basic characteristics

The texture in Estrup field is loam, with clay contents ranging from 0.055 to 0.140 kg kg^{-1} (Table 1). The field has a strong gradient in organic carbon content (OC) from 0.018 to 0.084 kg kg^{-1} (Fig. 1C). The highest OC is found in the south-western area of the field. The spatial distribution of clay can be found in Paradelo et al. (2015); the field presents higher clay contents in the north-eastern area and lower in the southern area. Bulk density varies from 1.02 to 1.59 g cm^{-3}, and showed a strong negative correlation with OC content (Table 2). The field provides an interesting wide range of soil characteristics to study air, water and solute flow characteristics.

CT-derived macroporosity, CT_{matrix} and genus density

Macroporosity was derived from the binary images after post processing. Figure 2 shows eight of the 45 studied columns, representing the entire range of 5% arrival time (further explained in the next section). The red colour represents macropores larger than 1.2 mm. In general, the macropores were well connected in both horizontal and vertical directions. The macroporosity varied greatly, ranging from 0.016 to 0.102 cm^3 cm^{-3}, similar to the range reported by Larsbo, et al. (2014) in samples from agricultural soils in Sweden. The vertical distribution of the macroporosity is shown in Figure 3A for depth intervals of 0.6 mm. The macroporosity varied greatly with depth, and the coefficients of variation for the individual columns ranged from 0.13 to 0.77. Different macroporosity profiles were found. For some columns, macroporosity decreased from top to bottom (e.g. #45), some presented higher macroporosity around -60 mm depth (e.g. #5, #17), while others presented higher macroporosity at top and bottom of the columns decreasing in the middle (e.g. #32, #35). Some studies have observed decreasing macroporosity with depth (Katuwal, et al., 2015b, Luo et al., 2010a, Naveed, et al., 2013), but it is not clear in the present study. Management practices before sampling can greatly influence macroporosity differences between fields. In a previous work (Katuwal, et al., 2015b) soil columns were sampled and scanned in a different field (Silstrup, Denmark) 26 months after the last ploughing (Norgaard et al., 2013), while in our study only 10 months elapsed between ploughing and sampling. This might result in higher macroporosity but with a less organized pore network. The limiting macroporosity was obtained from the 0.6 mm resolution macroporosity profiles and ranged from 0.02 to 0.068 $cm^3\ cm^{-3}$ (Table 1). The limiting macroporosity presented a higher coefficient of variation (47%) than the macroporosity (21%).

Macroporosity was positively correlated with clay content ($r = 0.318$, $p < 0.05$, Table 2, Fig. 4A), supporting the important role of clay in forming and maintaining macropore structures (Horn et al., 1994, Keller and Dexter, 2012). No other soil basic characteristics were significantly correlated with macroporosity (Table 2). When clay content is sufficient for the formation of soil aggregates, organic matter provides stability and helps maintain the soil structure (Schjonning et al., 2012). However, the stability of large aggregates (>2000 µm), responsible for macroporosity, is related to the growth of roots and hyphae (Tisdall and Oades, 1982), the presence of mesofauna, swelling-shrinkage processes (Jarvis, 2007) or the clay mineralogy (Denef and Six, 2005), and controlled by soil management. The macroporosity was poorly correlated with OC in Estrup ($r = -0.179$, Table 2, Fig. 4B) and hence with bulk density (Fig. 4C) in this particular case. Genus density was calculated to account the connectivity of the pore network. It varied from 0.120 to 1.176 and it was strongly correlated with macroporosity ($r = 0.937$, $p < 0.001$).

The CT_{matrix} was obtained from the greyscale 3D images discarding stones and macropores (>1.2 mm) (Table 1). High-density areas within the soil column can dramatically affect the flow of air and water through the soil, and CT images enable the identification of such areas (Jenssen and Heyerdahl, 1988). The depth distribution of the CT_{matrix} is shown in Fig. 3B. The

CT_{matrix} increased with depth until about 60–100 mm, after which it remained constant or slightly increased. For some of the columns, a decrease in CT_{matrix} was found at the bottom (160-170 mm). This decrease was probably caused by disturbances during sampling and handling of the soil columns. The small variability along the column depth, with CV < 0.15, suggested that for this study it would not be relevant to determine the maximum CT_{matrix} and its depth.

As expected, the CT_{matrix} showed a strong, positive correlation with bulk density ($r = 0.811$, $p < 0.001$) (Fig. 4E). In this field, OC controls the variation in bulk density, and therefore OC was also strongly correlated with CT_{matrix} ($r = -0.691$, $p < 0.001$) (Fig. 4F).

Relationship between CT-derived parameters and solute transport

Forty four tracer BTCs were collected from the solute transport experiments; for column #2 the BTC could not be obtained because water ponded on the surface of the column during the experiment. Figure 2 shows eight BTC examples, together with their corresponding 3D macropore renderings, covering the wide range of BTC shapes observed for the 44 samples. Some BTCs were highly skewed to the right, with the concentration peak achieved in less than one hour (*i.e.* #32, #35). This behaviour reflected preferential flow through the column. It is expected that preferential flow is associated with the presence of macropores well-connected in the vertical direction but poorly connected in the horizontal plane (Jarvis, 2007), but the visual inspection of the 3D macropore renderings for columns #32 and #35 did not show any special features that were different from the remaining samples.

Table 1 shows the BTC shape measures obtained by fitting the double-lognormal PDF. The mean value of $t_{0.05}$ was 2.24 h (s.d. = 0.92 h). The maximum value of $t_{0.05}$ was obtained for #15 (5.21 h) and the minimum for #35 (0.42 h). The apparent dispersivity ranged from 0.92 cm (#15) to 5.77 cm (#35), with a mean value of 2.32 cm (s.d. = 1.35 cm). The CT_{matrix} showed the best correlations with the BTCs' shape measures, $t_{0.05}$ ($r = -0.717$, $p < 0.001$) and λ_{app} ($r = 0.655$, $p < 0.001$) (Table 2). The 5% arrival time showed the best linear relationship with CT_{matrix} (Fig. 5A). The relationship between $t_{0.05}$ and λ_{app} followed a power function with $R^2 > 0.8$ (plot not shown). The power function improved the relationship between λ_{app} and CT_{matrix} (Fig. 5C). However, it was not better than the linear relationship between $t_{0.05}$ and CT_{matrix}.

Neither macroporosity nor limiting macroporosity were able to explain the variability in $t_{0.05}$ and λ_{app} better than CT_{matrix} (Table 2). The right-hand panels in Fig. 5 show the relationships between the BTC shape measurements ($t_{0.05}$ and λ_{app}) and limiting macroporosity. Katuwal, et al. (2015b) found that lower limiting macroporosity produced a higher degree of preferential flow, but here we could not find any strong correlation.

Preferential flow normally occurs when the soil is close to saturation and the macropores are conductive. The degree of saturation (S) during steady state flow ranged between 0.68 and 0.95 (Table 1) for the boundary conditions defined in this study (constant irrigation of 10 mm h^{-1} and seepage face at the bottom of the column). We observed higher degree of preferential flow in soil columns closer to saturation, stated by the significant correlations of S with $t_{0.05}$ and λ_{app} (Table 2). These results are in line with previous studies (Ghafoor et al., 2013, Katuwal, et al., 2015a, Koestel, et al., 2013, Larsbo, et al., 2014). The degree of saturation was significantly negatively correlated with macroporosity and positively correlated with CT_{matrix} (Table 2). Larger macroporosities and less dense soil matrix prevented soils from saturation at the experimental conditions. Larsbo, et al. (2014) found that larger macroporosities reduced the degree of preferential flow because they present large near-saturated conductivities that inactivate macropores at steady near-saturated steady flow.

In order to know when the macropores larger than 1.2 mm act as preferential flow paths we plotted $t_{0.05}$ as function of the water in the macropores (Fig. 6A) and the degree of saturation of the macropores (Fig. 6B). The water in the macropores was calculated as the difference between macroporosity and the air filled porosity during leaching. If this value is negative the macropores remain empty during the leaching experiment while a positive value means that water flowed through the macropores; for the samples where water was present in the macropores the degree of saturation of the macropores was calculated by dividing the latter by the macroporosity. We can observe that $t_{0.05}$ decreased with increasing the amount of water in the macropores. Dividing the data in two groups regarding macroporosity (higher and lower than 0.07 mm^3 mm^{-3}) we observed that $t_{0.05}$ was slightly affected by the amount of water in the macropores for large macroporosities, but strongly affected in soil columns with low macroporosities (R^2 = 0.62). Furthermore, low macroporosities lead to both the shortest (samples #32, #35) and the largest (samples #15, #9) arrival times. Thus, the differences in solute transport are controlled by the macropore networks lower than 1.2 mm lumped in the quantification of CT_{matrix} (Katuwal, et al., 2015a). Samples with denser matrix would have higher water potential during leaching experiment activating the macropore flow paths. If the macropore network is large and well-connected in both the horizontal and the vertical directions the degree of saturation of the macropores will be low (Fig 6B) decreasing the degree of preferential flow. For lower macroporosities the degree of saturation of the macropores is higher, acting as preferential flow paths. The water potential in the looser soil matrices were below the water saturation for an intensity of 10 mm h^{-1} and therefore the transport of the tracer is controlled by matrix flow rather than macropore flow. Thus, the calculation of the CT_{matrix} helped to explain the occurrence of different flow regimes at near saturated steady state flow and it would be an interesting proxy variable for modelling solute transport. However, improving resolution of the CT images will help to define better the macropore networks involved in this process. The boundary conditions will also play an important role in controlling the degree of saturation of the matrix and the macropores. Vogel et al. (2006) already suggested that a representation of the structure using the three-dimensional topology and the hydraulic properties of the material are necessary to predict solute transport and flow. In analogy with our study the macroporosity would represent the structure and the CT_{matrix} would give us information of the hydraulic properties of the soil matrix.

Relationships between CT-derived parameters and air permeability and saturated hydraulic conductivity

The air permeability of the soil columns was measured at *in situ* soil moisture conditions (around field capacity) and before the leaching experiments at -2 kPa matric potential at the centre of the column. The mean value for $K_{a\ (in\ situ)}$ was 89.6 µm^2 (s.d.= 44.9) and 68.6 µm^2 (s.d.= 49.8) for $K_{a\ (-2\ kPa)}$ (Table 1). The air permeabilities at $K_{a\ (in\ situ)}$ and $K_{a\ (-2\ kPa)}$ were correlated ($r = 0.487$, $p < 0.001$) (Table 2) and, as expected, $K_{a\ (in\ situ)}$ was higher than $K_{a\ (-2\ kPa)}$ for most of the samples. However, some $K_{a\ (-2\ kPa)}$ values were higher than $K_{a\ (in\ situ)}$, probably due to the opening of clogged pores during handling in the laboratory. Macroporosity was positively correlated with $K_{a\ (in\ situ)}$ ($R^2 = 0.376$, $p < 0.05$) (Fig. 7A). Worse relationship was obtained between macroporosity and $K_{a\ (-2\ kPa)}$ ($R^2 = 0.114$, $p < 0.05$) (Fig. 7A). The matric potentials at which K_a was measured, equal to or lower than -2 kPa, pores of 0.15 mm diameter, and even smaller, were air filled (see water contents in Table1). The difference between the pores accounted by CT-images (larger than 1.2 mm) and the actual air-filled pores can be responsible for the lack of correlation. The limiting macroporosity improved slightly the linear relationships with the air permeabilities (Fig. 7B, 7D). Limiting macroporosity helped to detect layers in the soil where the advective flow was restricted and cannot be accounted by the average macroporosity. Naveed, et al. (2013) and Katuwal, et al. (2015b) also report better correlations of $K_{a\ (-2kPa)}$ using limiting macroporosity; R^2 increased from 0.88 to 0.93 and from 0.78 to 0.82 respectively.

Saturated hydraulic conductivity (K_{sat}), measured after the leaching experiments, followed a lognormal distribution (not shown), with values ranging from 0.05 to 25.91 cm h^{-1}. The skewed distribution of soil characteristics, and in particular K_{sat}, is frequently reported in the literature (Iqbal et al., 2005, Warrick and Nielsen, 1980). The variability in K_{sat} is in line with the different degrees of saturation S during the leaching experiment (Table 2). Lower K_{sat} led to higher S and, as we stated before, macropores become preferential flow paths.

The K_{sat} showed significant but low linear correlations with macroporosity and limiting macroporosity (Figure 7E, F) indicating that not only the pores higher than 1.2 mm control water flow at saturated conditions. Indeed, the correlation between CT_{matrix} and K_{sat} ($r = -0.529$, $p < 0.001$, Table 2) suggests that matrix flow had a big influence in K_{sat}. Luo, et al. (2010b) reported differences in the slope of the linear relationship between $\log_{10}(K_{sat})$ and macroporosity between cropland and pasture soils (54.03 and 37.68 respectively). They found that macropores in croplands were less tortuous and vertically oriented; thus a small increase in macroporosity produced a significant increase in K_{sat}. In the present study, the slope between $\log_{10}(K_{sat})$ and macroporosity was 12. Thus the macropores in Estrup were horizontally well connected (Fig. 2). The relatively short time for the development of the soil structure after the last ploughing (10 months) together with its low clay content could reduce the presence of vertically connected macropores.

Combining CT-derived characteristics to explain air, water and solute transport

Best subsets linear regressions were performed to find the models that explained $t_{0.05}$, $K_{a\ (in\ situ)}$ and $\log_{10}(K_{sat})$ best using CT-derived characteristics. The best models for $t_{0.05}$, $K_{a\ (in\ situ)}$ and $\log_{10}(K_{sat})$ are shown in Table 3. None of the best models included macroporosity, limiting macroporosity and genus density due to the high correlation between them. The best subset models improved the predictions for $K_{a\ (in\ situ)}$ and $log_{10}(K_{sat})$ compared with the single linear models. For $t_{0.05}$ the best model used only CT_{matrix}. No improvement was found by introducing macroporosity or limiting macroporosity.

Genus density and CT_{matrix} were selected in the best model for $K_{a\ (in\ situ)}$ (R^2 = 0.613, Table 3). It should be pointed out that the model for $K_{a\ (in\ situ)}$ that includes limiting macroporsity and CT_{matrix} was as good as the best model (R^2= 0.610). Limiting macroporosity and CT_{matrix} were selected for $log_{10}(K_{sat})$ (R^2 = 0.448). This confirmed that air and water flows follow the same paths through the soil (Iversen, et al., 2001a, Loll et al., 1999). The use of limiting macroporosity and genus density in the prediction models can give an idea of the importance of macropore connectivity in water and air transport. Macroporosity and the path number (paths going from the top to the bottom of the soil sample, representing the vertical connectivity of the sample) have been found by Luo, et al. (2010b) to be good predictors of K_{sat}.

The residuals were generally well distributed along the 1:1 line (Fig. 8). For the $K_{a\ (in\ situ)}$ model, the residuals were well distributed along the 1:1 line, but exhibited larger scatter than $t_{0.05}$. Only sample #15 deviated from the $t_{0.05}$ model. Since limiting macroporosity had a greater influence on $K_{a\ (in\ situ)}$, the identification of pores smaller than 1.2 mm would help to reduce this scatter. A slight overestimation at low values (*i.e.* #35) and underestimation at high values could be observed in the $log_{10}(K_{sat})$ model. Luo, et al. (2010b) obtained better predictions of K_{sat} using the path number and macroporosity in their multiple linear regression analysis. For Estrup, the path number and other parameters related with macropore connectivity were not correlated with K_{sat}. The lower clay content compared with other studies and the shorter time for structure development could be the reason for lower predictability of K_{sat}.

CONCLUSIONS

The CT-derived parameters macroporosity, CT_{matrix} and Genus density were used to explain solute, water and air transport at field scale. The studied field in Estrup, Denmark, presented a pronounced gradient in OC content which controlled the variability in bulk density in the field. Consequently, OC presented a high correlation with CT_{matrix}. Clay content was the soil property that correlated best with macroporosity, confirming the importance of clay in building and maintaining soil macropores. CT_{matrix} presented the best correlations with the $t_{0.05}$. The matrix density controls the degree of saturation of the matrix and the macropores and hence the degree of preferential flow. The relationships found are highly dependent of the boundary and initial conditions since they control the degree of saturation and the activation of macropores as preferential flow paths. Limiting macroporosity presented the highest correlations with K_a, both at *in situ* soil moisture conditions and at -2kPa, and $\log_{10}(K_{sat})$. These results suggest that the layers with the fewest macropores restrict the flow for the whole soil column. Combining macroporosity, limiting macroporosity, genus density and CT_{matrix} improved the regression coefficients with water and air flow, but some uncertainties have not been solved yet. Intensive multivariate analyses can be done using techniques that cope with the multicollinearity of the CT-derived parameters like partial least square regression. However, bigger and standardized datasets are needed to obtain reliable models.

ACKNOWLEDGMENTS

The study was financed by the international project Soil Infrastructure, Interfaces and Translocation Processes in Inner Space (Soil-it is) funded by the Danish Research Council for Technology and Production Sciences (http://www.agrsci.dk/soil-it-is/) and the Danish Pesticide Leaching Assessment Programme (www.pesticidvarsling.dk). M. Paradelo is supported by a postdoctoral contract from Plan I2C, Xunta de Galicia. The authors gratefully acknowledge the technical support provided by Stig T. Rasmussen, Michael Koppelgaard, and Palle Jorgensen.

REFERENCES

Abramoff, M.D., P.J. Magalhaes and S.J. Ram. 2004. Image Processing with ImageJ. Biophotonics International 11: 36-42.

Anderson, S.H., C.J. Gantzer, J.M. Boone and R.J. Tully. 1988. Rapid Nondestructive Bulk Density and Soil-Water Content Determination by Computed Tomography. Soil Sci Soc Am J 52: 35-40. doi:10.2136/sssaj1988.03615995005200010006x.

Ball, B.C. 1981. Pore characteristics of soils from two cultivation experiments as shown by gas diffusivities and permeabilities and air-filled porosities. J Soil Sci 32: 483-498.

de Jonge, L.W., C. Kjaergaard and P. Moldrup. 2004a. Colloids and colloid-facilitated transport of contaminants in soils: An introduction. Vadose Zone J 3: 321-325. doi:10.2136/vzj2004.0321.

de Jonge, L.W., P. Moldrup, G.H. Rubaæk, K. Schelde and J. Djurhuus. 2004b. Particle leaching and particle-facilitated transport of phosphorus at field scale. Vadose Zone J 3: 462-470.

Denef, K. and J. Six. 2005. Clay mineralogy determines the importance of biological versus abiotic processes for macroaggregate formation and stabilization. Eur J Soil Sci 56: 469-479. doi:10.1111/j.1365-2389.2004.00682.x.

Doube, M., M.M. Kłosowski, I. Arganda-Carreras, F.P. Cordelières, R.P. Dougherty, J.S. Jackson, et al. 2010. BoneJ: Free and extensible bone image analysis in ImageJ. Bone 47: 1076-1079. doi:10.1016/j.bone.2010.08.023.

Ferreira, T. and W. Rasband. 2012. ImageJ User Guide - IJ 1.46r. National Institute of Health, Bethesda,MD.

Gee, G.W. and D. Or. 2002. Particle-size analysis. In: J. H. Dane and G. C. Topp, editors, Methods of soil analysis. Part 4. SSSA Book Series No. 5. . SSSA, Madison, WI. p. 255-293.

Ghafoor, A., J. Koestel, M. Larsbo, J. Moeys and N. Jarvis. 2013. Soil properties and susceptibility to preferential solute transport in tilled topsoil at the catchment scale. J Hydrol 492: 190-199. doi:10.1016/j.jhydrol.2013.03.046.

Helliwell, J.R., C.J. Sturrock, K.M. Grayling, S.R. Tracy, R.J. Flavel, I.M. Young, et al. 2013. Applications of X-ray computed tomography for examining biophysical interactions and structural development in soil systems: a review. Eur J Soil Sci 64: 279-297. doi:Doi 10.1111/Ejss.12028.

Hocking, R.R. 1976. A Biometrics Invited Paper. The Analysis and Selection of Variables in Linear Regression. Biometrics 32: 1-49. doi:10.2307/2529336.

Horn, R., H. Taubner, M. Wuttke and T. Baumgartl. 1994. Soil physical properties related to soil structure. Soil and Tillage Research 30: 187-216. doi:http://dx.doi.org/10.1016/0167-1987(94)90005-1.

Iqbal, J., J.A. Thomasson, J.N. Jenkins, P.R. Owens and F.D. Whisler. 2005. Spatial Variability Analysis of Soil Physical Properties of Alluvial Soils This study was in part supported by The National Aeronautical and Space Administration funded Remote Sensing Technology Center at Mississippi State University. Soil Sci. Soc. Am. J. 69: 1338-1350. doi:10.2136/sssaj2004.0154.

Iversen, B.V., M. Lamande, S.B. Torp, M.H. Greve, G. Heckrath, L.W. de Jonge, et al. 2012. Macropores and Macropore Transport: Relating Basic Soil Properties to Macropore Density and Soil Hydraulic Properties. Soil Sci 177: 535-542. doi:10.1097/SS.0b013e31826dd155.

Iversen, B.V., P. Moldrup, P. Schjonning and P. Loll. 2001a. Air and water permeability in differently textured soils at two measurement scales. Soil Sci 166: 643-659. doi:Doi 10.1097/00010694-200110000-00001.

Iversen, B.V., P. Schjonning, T.G. Poulsen and P. Moldrup. 2001b. In situ, on-site and laboratory measurements of soil air permeability: Boundary conditions and measurement scale. Soil Sci 166: 97-106. doi:Doi 10.1097/00010694-200102000-00003.

Jarvis, N.J. 2007. A review of non-equilibrium water flow and solute transport in soil macropores: principles, controlling factors and consequences for water quality. Eur J Soil Sci 58: 523-546. doi:10.1111/j.1365-2389.2007.00915.x.

Jarvis, N.J., J. Moeys, J.M. Hollis, S. Reichenberger, A.M.L. Lindahl and I.G. Dubus. 2009. A conceptual model of soil susceptibility to macropore flow. Vadose Zone J 8: 902-910. doi:10.2136/vzj2008.0137.

Jenssen, P.D. and P.H. Heyerdahl. 1988. Soil Column Descriptions from X-Ray Computed-Tomography Density Images. Soil Sci 146: 102-107. doi:10.1097/00010694-198808000-00007.

Jury, W.A. and K. Roth. 1990. Transfer functions and solute movement through soil: theory and applicationsBirkhäuser Verlag.

Katuwal, S., P. Moldrup, M. Lamandé, M. Tuller and L.W. de Jonge. 2015a. Effects of CT Number-Derived Matrix Density on Preferential Flow and Transport in Macroporous Agricultural Soils. Vadose Zone J In press. doi:10.2136/v15.01.0002.

Katuwal, S., T. Norgaard, P. Moldrup, M. Lamande, D. Wildenschild and L.W. de Jonge. 2015b. Linking air and water transport in intact soils to macropore characteristics inferred from X-ray computed tomography. Geoderma 237: 9-20. doi:DOI 10.1016/j.geoderma.2014.08.006.

Keller, T. and A.R. Dexter. 2012. Plastic limits of agricultural soils as functions of soil texture and organic matter content. Soil Research 50: 7-17.

Ketcham, R.A. and W.D. Carlson. 2001. Acquisition, optimization and interpretation of X-ray computed tomographic imagery: applications to the geosciences. Comput. Geosci. 27: 381-400. doi:10.1016/s0098-3004(00)00116-3.

Klute, A. and C. Dirksen. 1986. Hydraulic Conductivity and Diffusivity: Laboratory Methods. In: A. Klute, editor Methods of Soil Analysis: Part 1—Physical and Mineralogical Methods. Soil Science Society of America, American Society of Agronomy. p. 687-734.

Knudby, C. and J. Carrera. 2005. On the relationship between indicators of geostatistical, flow and transport connectivity. Adv Water Resour 28: 405-421. doi:10.1016/j.advwatres.2004.09.001.

Koestel, J. and H. Jorda. 2014. What determines the strength of preferential transport in undisturbed soil under steady-state flow? Geoderma 217-218: 144-160. doi:10.1016/j.geoderma.2013.11.009.

Koestel, J.K., J. Moeys and N.J. Jarvis. 2011. Evaluation of Nonparametric Shape Measures for Solute Breakthrough Curves. Vadose Zone J 10: 1261-1275. doi:10.2136/Vzj2011.0010.

Koestel, J.K., T. Norgaard, N.M. Luong, A.L. Vendelboe, P. Moldrup, N.J. Jarvis, et al. 2013. Links between soil properties and steady-state solute transport through cultivated topsoil at the field scale. Water Resour Res 49: 790-807. doi:Doi 10.1002/Wrcr.20079.

Larsbo, M., J. Koestel and N. Jarvis. 2014. Relations between macropore network characteristics and the degree of preferential solute transport. Hydrol Earth Syst Sc 18: 5255-5269. doi:DOI 10.5194/hess-18-5255-2014.

Lindhardt, B., C. Abildtrup, H. Vosgerau, P. Olsen, S. Torp, B.V. Iversen, et al. 2001. The Danish Pesticide Leaching Assessment Programme: Site characterization and monitoring design.Geological Survey of Denmark and Greenland, Copenhagen, Denmark.

Loll, P., P. Moldrup, P. Schjonning and H. Riley. 1999. Predicting saturated hydraulic conductivity from air permeability: Application in stochastic water infiltration modeling. Water Resour Res 35: 2387-2400. doi:10.1029/1999wr900137.

Luo, L.F., H. Lin and S.C. Li. 2010a. Quantification of 3-D soil macropore networks in different soil types and land uses using computed tomography. J Hydrol 393: 53-64. doi:10.1016/j.jhydrol.2010.03.031.

Luo, L.F., H. Lin and J. Schmidt. 2010b. Quantitative Relationships between Soil Macropore Characteristics and Preferential Flow and Transport. Soil Sci Soc Am J 74: 1929-1937. doi:10.2136/sssaj2010.0062.

McCarthy, J.F. and J.M. Zachara. 1989. Subsurface transport of contaminants. Mobile colloids in the subsurface environment may alter the transport of contaminants. Environmental Science and Technology 23: 496-502. doi:10.1021/es00063a001.

Naveed, M., P. Moldrup, E. Arthur, D. Wildenschild, M. Eden, M. Lamand, et al. 2013. Revealing Soil Structure and Functional Macroporosity along a Clay Gradient Using X-ray Computed Tomography. Soil Sci Soc Am J 77: 403-411. doi:10.2136/sssaj2012.0134.

Norgaard, T., P. Moldrup, T.P.A. Ferre, P. Olsen, A.E. Rosenbom and L.W. de Jonge. 2014. Leaching of Glyphosate and Aminomethylphosphonic Acid from an Agricultural Field over a Twelve-Year Period. Vadose Zone J 13. doi:DOI 10.2136/vzj2014.05.0054.

Norgaard, T., P. Moldrup, P. Olsen, A.L. Vendelboe, B.V. Iversen, M.H. Greve, et al. 2013. Comparative Mapping of Soil Physical-Chemical and Structural Parameters at Field Scale to Identify Zones of Enhanced Leaching Risk. J Environ Qual 42: 271-283. doi:10.2134/Jeq2012.0105.

Paradelo, M., P. Moldrup, E. Arthur, M. Naveed, M. Holmstrup, J.E. Lopez-Periago, et al. 2013. Effects of Past Copper Contamination and Soil Structure on Copper Leaching from Soil. J Environ Qual 42: 1852-1862. doi:10.2134/jeq2013.05.0209.

Paradelo, M., T. Norgaard, P. Moldrup, T.P.A. Ferre, K.G.I.D. Kumari, E. Arthur, et al. 2015. Prediction of the glyphosate sorption coefficient across two loamy agricultural fields. Goderma submited.

Roseberg, R.J. and E.L. Mccoy. 1990. Measurement of Soil Macropore Air Permeability. Soil Sci Soc Am J 54: 969-974.

Sauvola, J. and M. Pietikäinen. 2000. Adaptive document image binarization. Pattern Recognition 33: 225-236. doi:http://dx.doi.org/10.1016/S0031-3203(99)00055-2.

Schelde, K., L.W. De Jonge, C. Kjaergaard, M. Laegdsmand and G.H. Rubæk. 2006. Effects of manure application and plowing on transport of colloids and phosphorus to tile drains. Vadose Zone J 5: 445-458. doi:10.2136/vzj2005.0051.

Schjonning, P., L.W. de Jonge, L.J. Munkholm, P. Moldrup, B.T. Christensen and J.E. Olesen. 2012. Clay Dispersibility and Soil Friability-Testing the Soil Clay-to-Carbon Saturation Concept. Vadose Zone J 11. doi:Doi 10.2136/Vzj2011.0067.

Soil Survey Staff. 1999. Soil Taxonomy. A basic system of soil classification for making and interpreting soil surveys. 2nd Edition ed. Natural Resources Conservation Service, USDA, Washington DC, USA.

Taina, I.A., R.J. Heck and T.R. Elliot. 2008. Application of X-ray computed tomography to soil science: A literature review. Can J Soil Sci 88: 1-20. doi:10.4141/CJSS06027.

Tisdall, J.M. and J.M. Oades. 1982. Organic-Matter and Water-Stable Aggregates in Soils. J Soil Sci 33: 141-163. doi:10.1111/j.1365-2389.1982.tb01755.x.

Traub-Eberhard, U., K.P. Henschel, W. Kordel and W. Klein. 1995. Influence of different field sites on pesticide movement into subsurface drains. Pestic Sci 43: 121-129. doi:10.1002/ps.2780430205.

Vaz, C.M.P., I.C. De Maria, P.O. Lasso and M. Tuller. 2011. Evaluation of an advanced benchtop Micro-Computed Tomography system for quantifying porosities and pore-size distributions of two Brazilian Oxisols. Soil Sci Soc Am J 75: 832-841. doi:10.2136/sssaj2010.0245.

Vogel, H.J., I. Cousin, O. Ippisch and P. Bastian. 2006. The dominant role of structure for solute transport in soil: experimental evidence and modelling of structure and transport in a field experiment. Hydrol Earth Syst Sc 10: 495-506.

Vogel, H.J., U. Weller and S. Schluter. 2010. Quantification of soil structure based on Minkowski functions. Comput. Geosci. 36: 1236-1245. doi:10.1016/j.cageo.2010.03.007.

Warrick, A.W. and D.R. Nielsen. 1980. Spatial variability of soil physical properties in the field. Applications of Soil Physics: 319-344.

Werth, C.J., C.Y. Zhang, M.L. Brusseau, M. Oostrom and T. Baumann. 2010. A review of non-invasive imaging methods and applications in contaminant hydrogeology research. J Contam Hydrol 113: 1-24. doi:10.1016/j.jconhyd.2010.01.001.

Wildenschild, D., J.W. Hopmans, C.M.P. Vaz, M.L. Rivers, D. Rikard and B.S.B. Christensen. 2002. Using X-ray computed tomography in hydrology: systems, resolutions, and limitations. J Hydrol 267: 285-297. doi:10.1016/S0022-1694(02)00157-9.

LIST OF FIGURES

Figure 7. Relationships of air permeability at in situ conditions ($K_{a\ (in\ situ)}$) and at -2 kPa ($K_{a\ (-2kPa)}$) and the logarithm of hydraulic conductivity ($\log_{10}(K_{sat})$) and CT-derived macroporosity and limiting macroporosity. Solid lines represent linear relationships. The R^2 values are presented only if the regression is significative ($p < 0.05$).

Figure 8. One-to-one plots of the best multiple linear regression models for A) 5% arrival time ($t_{0.05}$), B) air permeability at in situ conditions ($K_{a\ (in\ situ)}$), and C) the logarithm of saturated hydraulic conductivity ($\log_{10}(K_{sat})$). Solid lines represent 1:1 lines.

TABLES

Table 1. Soil and transport characteristics at Estrup field

	Mean (s.d.)	**min**	**max**
Clay (kg kg^{-1})	0.108 (0.021)	0.055	0.140
Silt (kg kg^{-1})	0.251 (0.034)	0.142	0.298
Sand (kg kg^{-1})	0.587 (0.058)	0.464	0.768
OC (kg kg^{-1})	0.03 (0.02)	0.018	0.084
Bulk density (Mg m^{-3})	1.39 (0.13)	1.02	1.59
$\theta_{(\text{in situ})}$ (cm^3 cm^{-3})	0.31(0.04)	0.22	0.41
$\theta_{(-2\ \text{kPa})}$ (cm^3 cm^{-3})	0.37 (0.04)	0.27	0.46
θ_l (cm^3 cm^{-3})	0.40 (0.03)	0.31	0.48
S (-)	0.85 (0.05)	0.68	0.94
$K_{a\ (\text{in situ})}$ (µm^2)	89.6 (44.9)	6.1	226.2
$K_{a(-2\ \text{kPa})}$ (µm^2)	68.6 (49.8)	1.3	241.3
K_s (cm h^{-1})	3.69 (5.33)	0.05	25.91
$t_{0.05}$ (h)	2.23 (0.92)	0.42	5.21
λ_{app} (cm)	2.33 (0.96)	0.92	5.77
Macroporosity (cm^3 cm^{-3})	0.066 (0.022)	0.016	0.102
Limiting macroporosity (cm^3 cm^{-3})	0.032 (0.015)	0.002	0.068
CT_{matrix} (HU)	867 (111)	589	1056
Genus density	0.566 (0.264)	0.120	1.176

1 Table 2. Spearman correlation matrix for soil basic characteristics, transport and CT-derived parameters

	Silt	Sand	OC	BD	$\theta_{in\ situ}$	$\theta_{(-2kPa)}$	θ_l	S	K_a	$K_{a\ (-2kPa)}$	K_s	$t_{0.05}$	λ_{app}	MPY	LimMPY	CT_{matrix}	Genus
Clay	0.514***	-0.512***	-0.382*	0.271	-0.153	-0.423**	-0.258	0.061	-0.007	0.066	-0.075	-0.438**	0.463**	0.318*	0.266	0.507***	0.277
Silt		-0.866***	0.023	0.044	0.118	-0.117	-0.049	-0.026	-0.185	-0.005	-0.049	-0.385**	0.402**	0.083	0.096	0.291	0.002
Sand			-0.319*	0.244	-0.414**	-0.204	-0.287	0.143	0.029	-0.047	-0.077	0.145	-0.256	-0.025	-0.146	-0.004	0.069
OC				-0.803***	0.817***	0.794***	0.803***	-0.26	0.182	0.181	0.254	0.349*	-0.212	-0.179	0.06	-0.691***	-0.211
BD					-0.637***	-0.691***	-0.749***	0.557***	-0.552***	-0.475**	-0.532***	-0.507***	0.398**	-0.245	-0.419**	0.811***	-0.187
θ_i						0.808***	0.882***	0.078	0.067	0.219	0.146	0.068	0.135	-0.314*	-0.011	-0.384*	-0.363*
θ_{20}							0.907***	0.026	0.154	0.106	0.172	0.364*	-0.154	-0.393**	-0.083	-0.613***	-0.398**
θ_l								0.029	0.258	0.25	0.25	0.243	-0.018	-0.226	0.045	-0.588***	-0.238
S									-0.561***	-0.312*	-0.518***	-0.551***	0.619***	-0.622***	-0.571***	0.573***	-0.564***
$K_{a\ (in\ situ)}$										0.487***	0.669***	0.465**	-0.427**	0.631***	0.682***	-0.526***	0.643***
$K_{a\ (-2kPa)}$											0.416**	0.152	-0.137	0.464**	0.500***	-0.266	0.344*
K_s												0.367*	-0.355*	0.455**	0.565***	-0.529***	0.435**
$t_{0.05}$													-0.921***	0.102	0.276	-0.717***	0.12
λ_{app}														-0.181	-0.242	0.655***	-0.212
MPY															0.818***	-0.082	0.937***
LimMPY																-0.263	0.762***
CT_{matrix}																	-0.097

OC: organic carbon content, BD: Bulk density, θ: water content at (in situ) in situ conditions, (-2kPa) at minus 2 kPa matric potential and (l) during leaching, S degree of saturation during leaching, K_a air permeability in situ conditions, (-2kPa) at minus 2 kPa matric potential, K_s: saturated hydraulic conductivity, $t_{0.05}$: 5% arrival time, λ_{app}: apparent dispersivity, MPY: macroporosity, LimMPY: limiting macroporosity, CT_{matrix}: CT number derived matrix density

Table 3. Best subset regression models for 5 % arrival time ($t_{0.05}$), air permeability *in situ* ($K_{a\ (in\ situ)}$) and the logarithm of saturated hydraulic conductivity ($\log_{10}(K_{sat})$) using CT-derived characteristics

Dependent variables	Best model equation	R^2	$Cp^{(1)}$	MS error	Standardized coefficients		
					CTmatrix	Limiting macroporosity	Genus density
$t_{0.05}$	$- 0.006\ CT_{matrix} + 7.49$	0.539	0.381	0.398	-0.734***		
$K_{a\ (in\ situ)}$	$-0.196\ CT_{matrix} + 98.75$ Genus density + 203.4	0.613	3.164	820	-0.485***		0.580***
$Log_{10}(K_{sat})$	$- 0.002\ CT_{matrix} + 16.91$ limiting macroporosity + 1.374	0.448	2.508	0.177	-0.386**	0.466***	

(1) Total squared error or Mallows's Cp

Figure 1

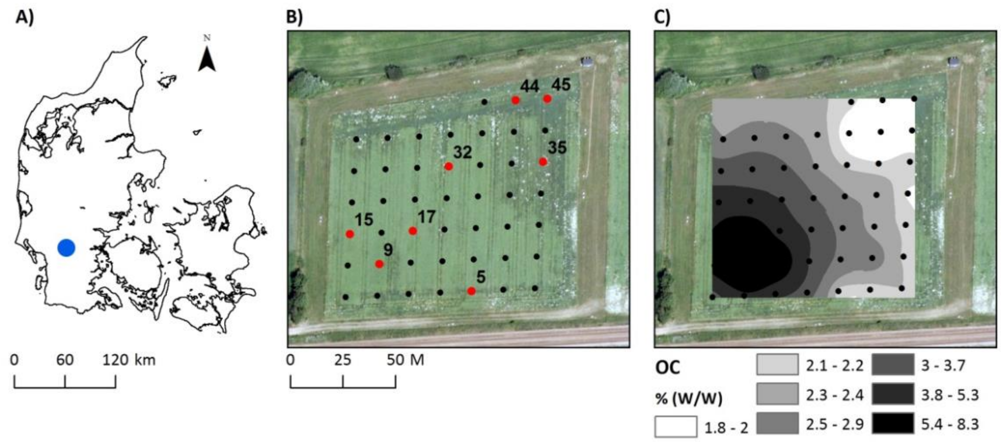

A)
B)
C)
44
45
32
35
15
17
9
5
0 60 120 km
0 25 50 M
OC
% (W/W)
1.8 - 2
2.1 - 2.2
2.3 - 2.4
2.5 - 2.9
3 - 3.7
3.8 - 5.3
5.4 - 8.3

Figure 2

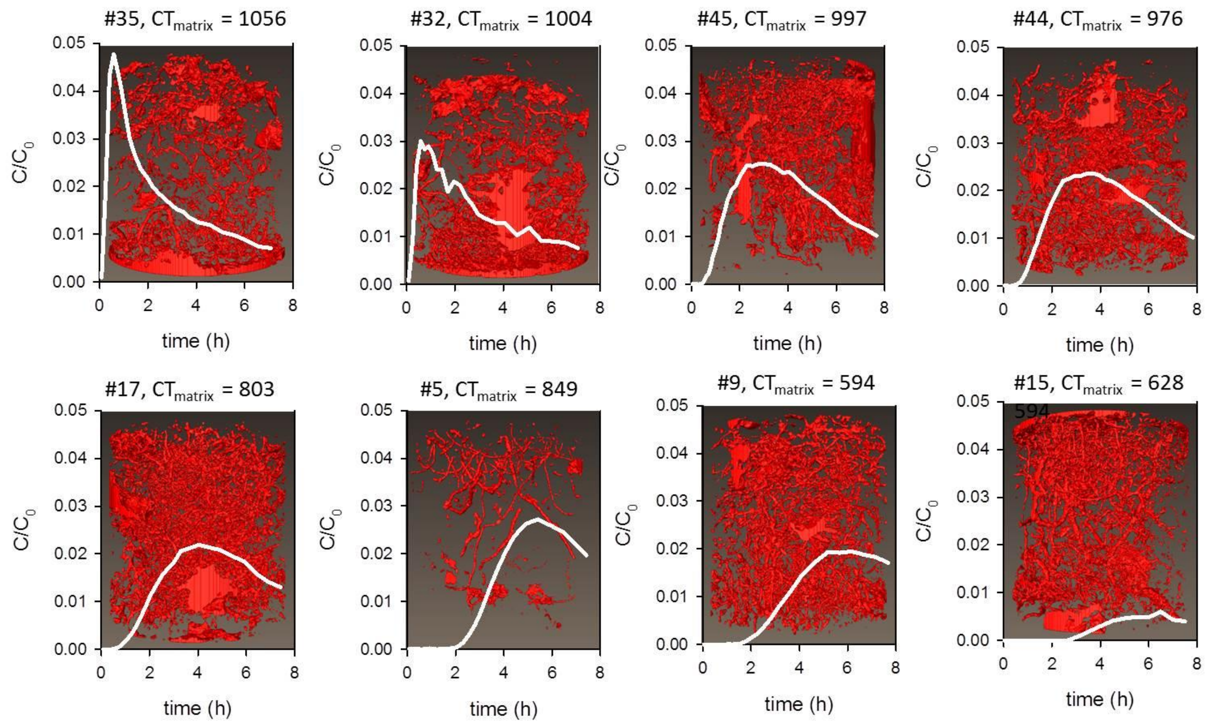

#35, CTmatrix = 1056
#32, CTmatrix = 1004
#45, CTmatrix = 997
#44, CTmatrix = 976
#17, CTmatrix = 803
#5, CTmatrix = 849
#9, CTmatrix = 594
#15, CTmatrix = 628
594
C/C0
time (h)
0.00
0.01
0.02
0.03
0.04
0.05
0
2
4
6
8

Figure 3

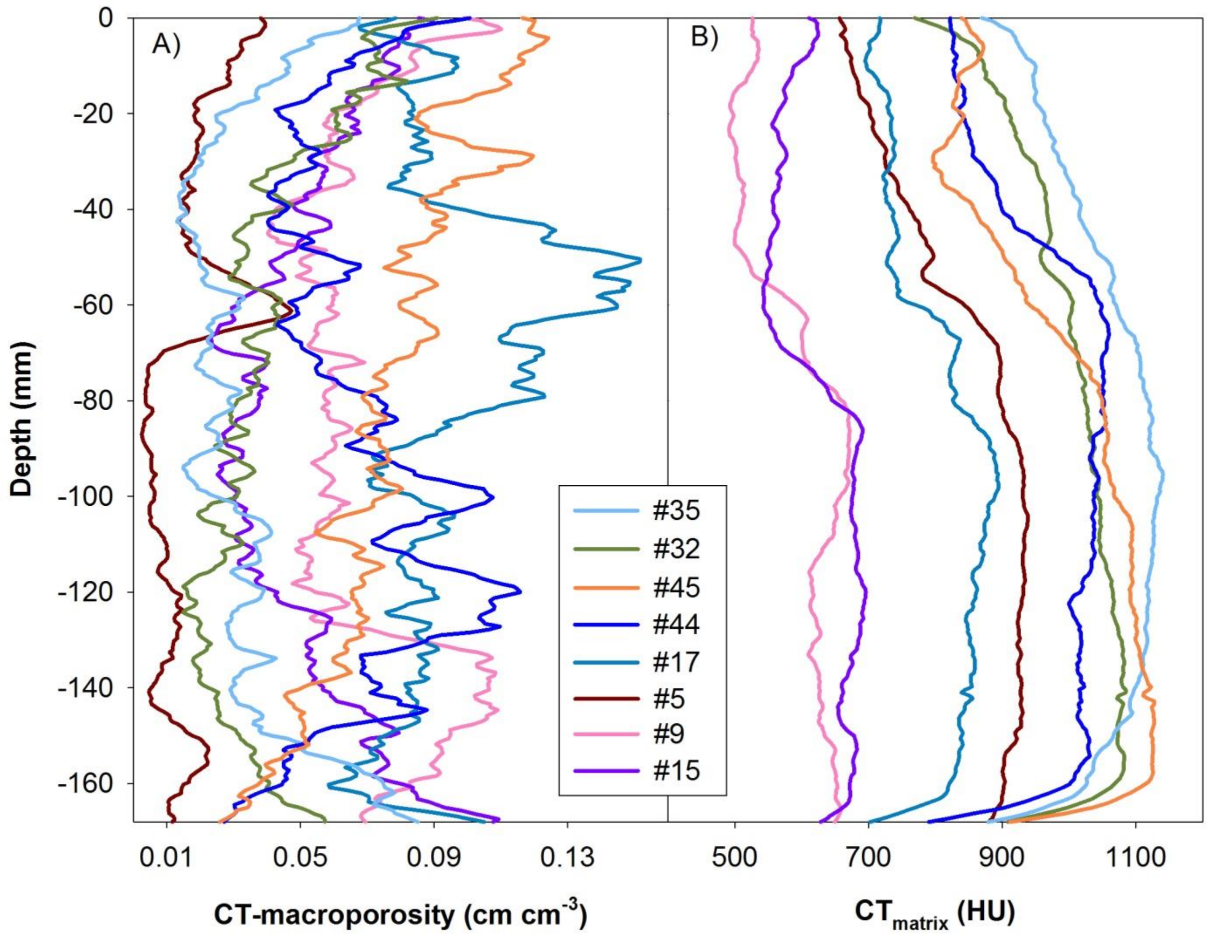

A)
B)
0
-20
-40
-60
-80
-100
-120
-140
-160
Depth (mm)
#35
#32
#45
#44
#17
#5
#9
#15
0.01
0.05
0.09
0.13
CT-macroporosity (cm cm-3)
500
700
900
1100
CTmatrix (HU)

Figure 4

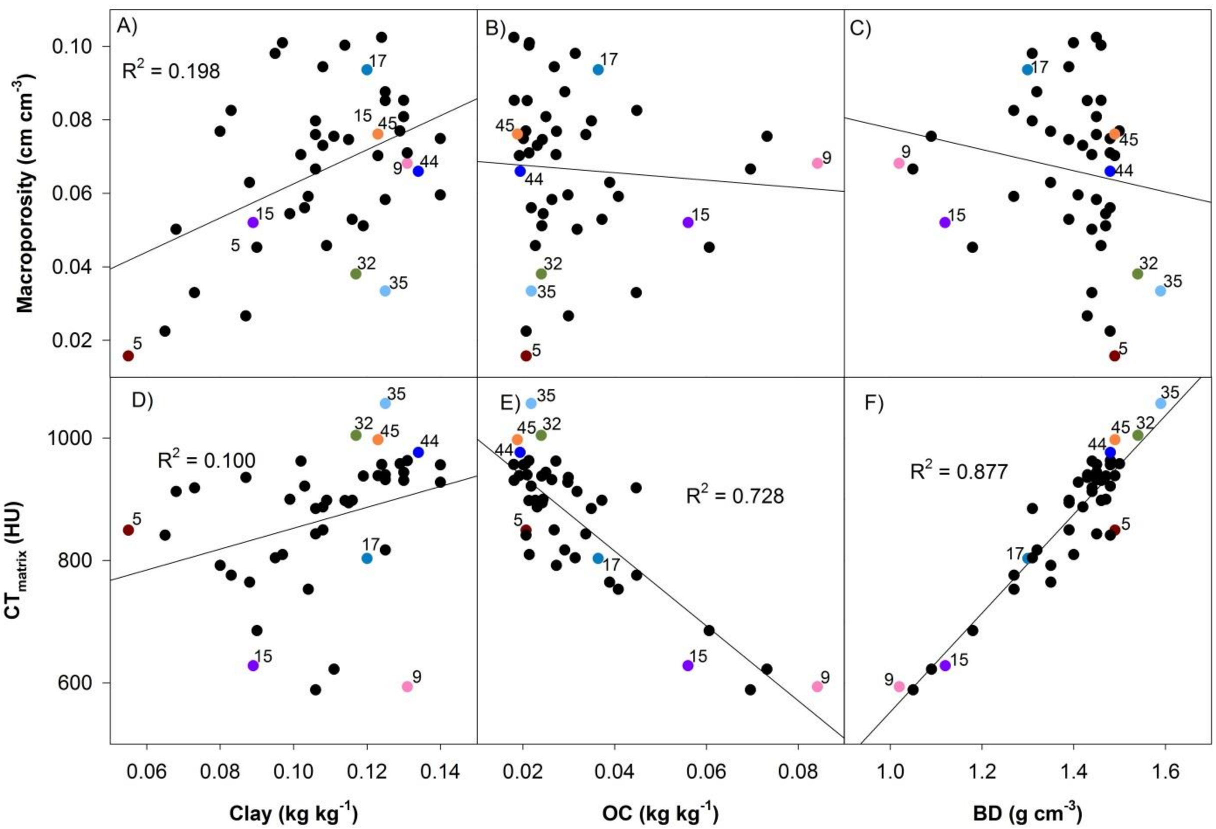

A)
B)
C)
D)
E)
F)
R^2 = 0.198
R^2 = 0.100
R^2 = 0.728
R^2 = 0.877
Macroporosity (cm cm^{-3})
CT_{matrix} (HU)
Clay (kg kg^{-1})
OC (kg kg^{-1})
BD (g cm^{-3})

Figure 5

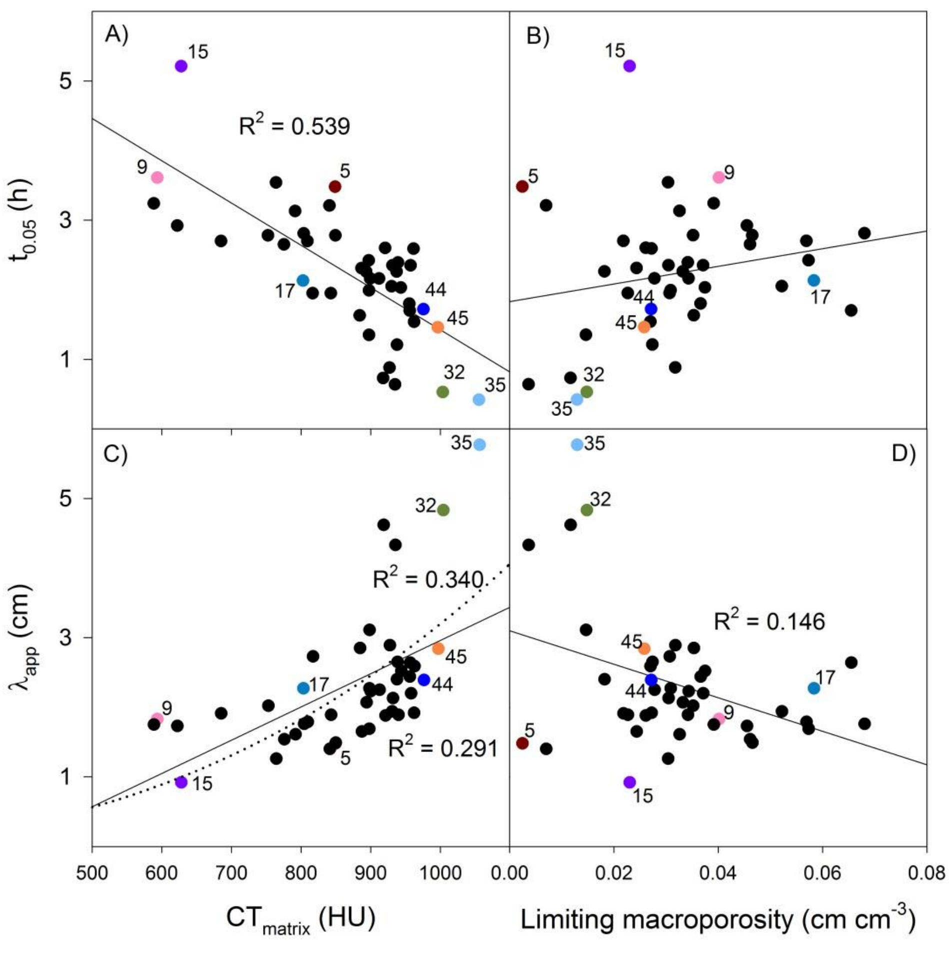

A)
B)
C)
D)
R^2 = 0.539
R^2 = 0.340
R^2 = 0.291
R^2 = 0.146
$t_{0.05}$ (h)
λ_{app} (cm)
CT_{matrix} (HU)
Limiting macroporosity (cm cm^{-3})

Figure 6

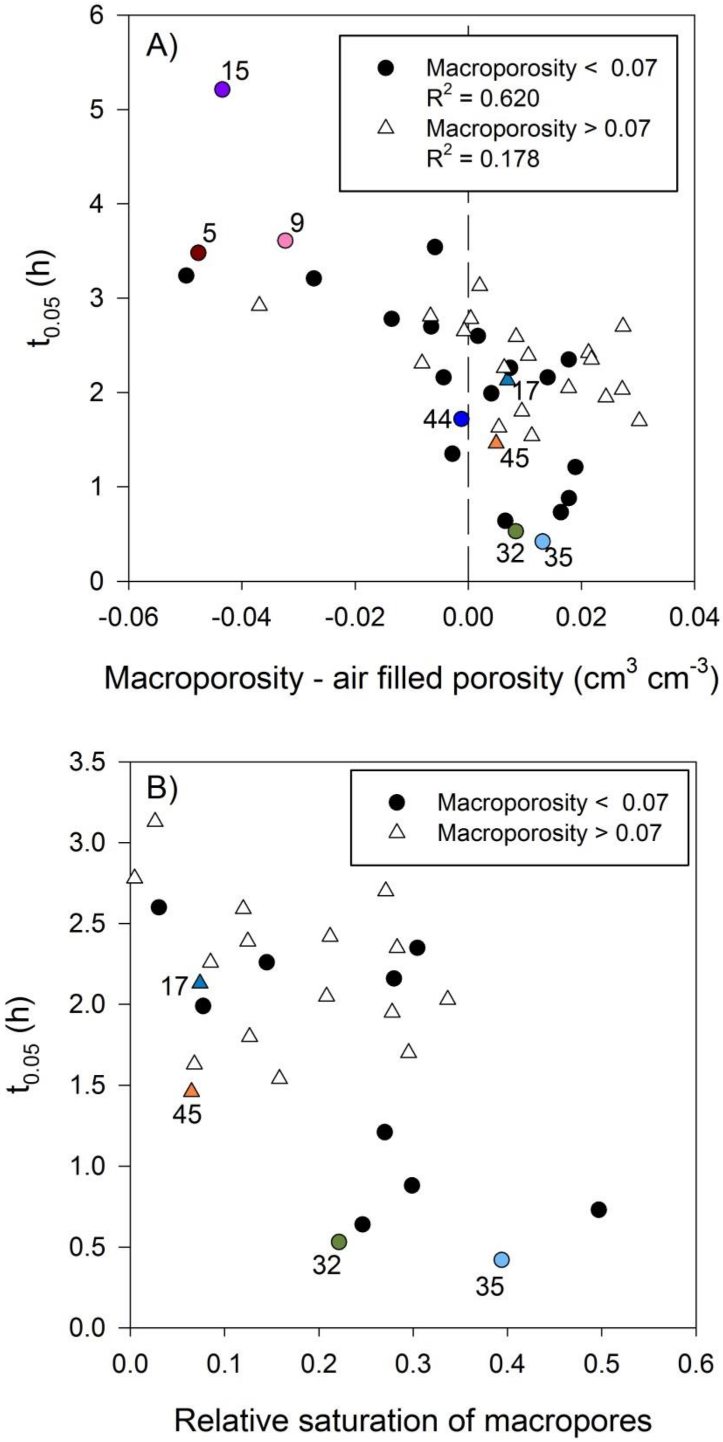
A)
Macroporosity < 0.07
R^2 = 0.620
Macroporosity > 0.07
R^2 = 0.178
15
5
9
17
44
45
32
35
$t_{0.05}$ (h)
Macroporosity - air filled porosity (cm^3 cm^-3)
B)
Macroporosity < 0.07
Macroporosity > 0.07
17
45
32
35
$t_{0.05}$ (h)
Relative saturation of macropores

Figure 7

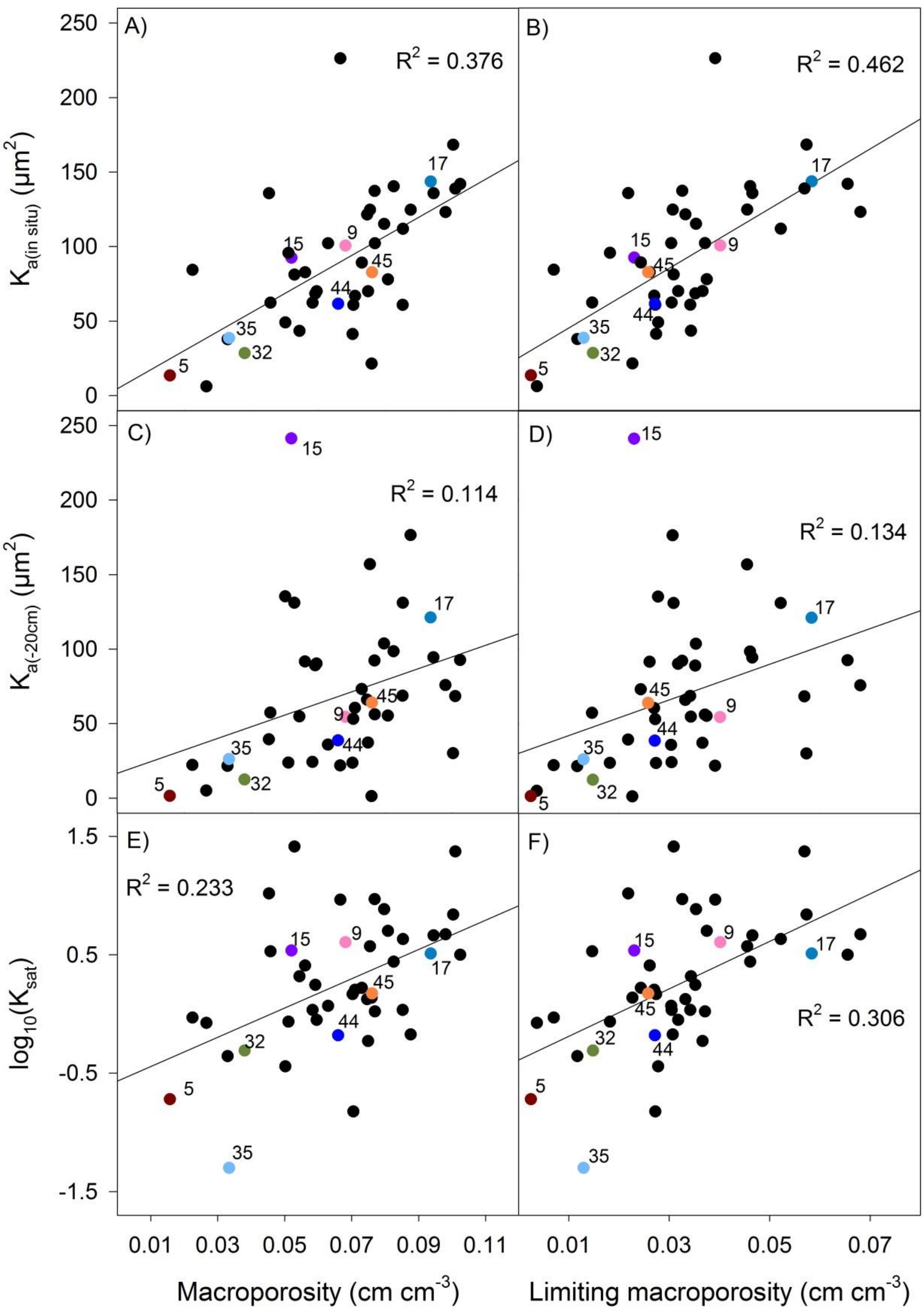

A)
R^2 = 0.376
B)
R^2 = 0.462
C)
R^2 = 0.114
D)
R^2 = 0.134
E)
R^2 = 0.233
F)
R^2 = 0.306
$K_{a(in\ situ)}$ (μm^2)
$K_{a(-20cm)}$ (μm^2)
$log_{10}(K_{sat})$
Macroporosity (cm cm^{-3})
Limiting macroporosity (cm cm^{-3})
0.01 0.03 0.05 0.07 0.09 0.11
0.01 0.03 0.05 0.07
250 200 150 100 50 0
1.5 0.5 -0.5 -1.5
5 9 15 17 32 35 44 45

Figure 8

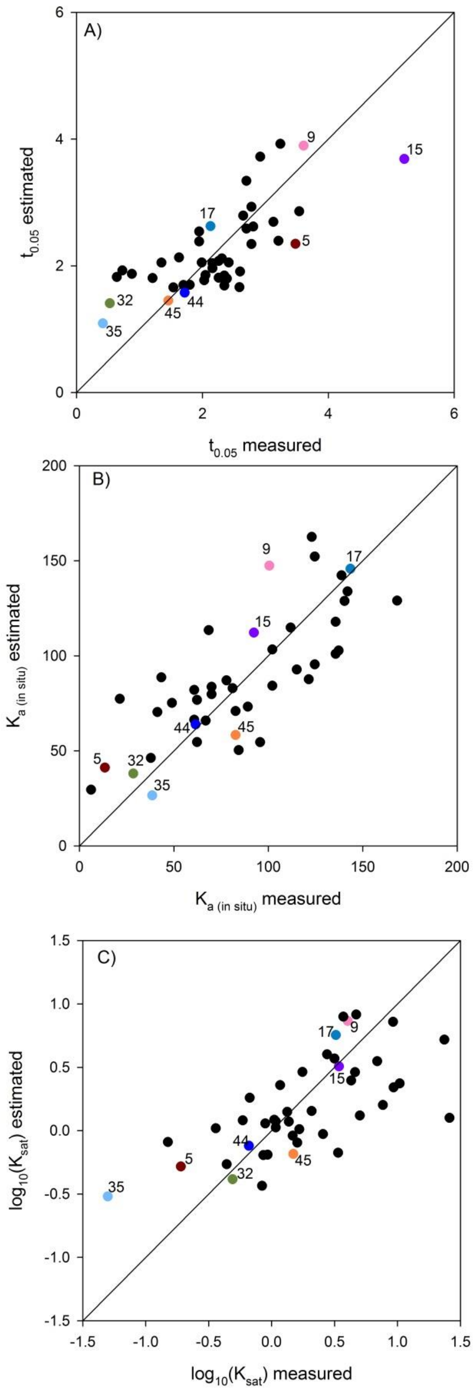
A)
$t_{0.05}$ estimated
$t_{0.05}$ measured
B)
$K_{a\ (in\ situ)}$ estimated
$K_{a\ (in\ situ)}$ measured
C)
$\log_{10}(K_{sat})$ estimated
$\log_{10}(K_{sat})$ measured